

# A 3.4–3.6 GHz High-Selectivity Filter Chip Based on Film Bulk Acoustic Resonator Technology

Qinghua Yang<sup>1</sup>, Yao Xu<sup>2</sup>, Yongle Wu<sup>2</sup> , Weimin Wang<sup>1,\*</sup> and Zhiguo Lai<sup>3</sup><sup>1</sup> School of Electronic Engineering, Beijing University of Posts and Telecommunications, Beijing 100876, China<sup>2</sup> School of Integrated Circuits, Beijing University of Posts and Telecommunications, Beijing 100876, China<sup>3</sup> Design Department, HunterSun Electronics Company Ltd., Suzhou 215000, China

\* Correspondence: wangwm@bupt.edu.cn

**Abstract:** The development of mobile 5G technology poses new challenges for high-frequency and high-performance filters. However, current commercial acoustic wave filters mainly focus on 4G LTE, which operates below 3 GHz. It is necessary to accelerate research on high-frequency acoustic wave filters. A high-selectivity film bulk acoustic resonator (FBAR) filter chip for the 3.4–3.6 GHz range was designed and fabricated in this paper. The design procedure includes FBAR parameter fitting, filter schematic analysis, and the generation principle of transmission zeros (TZs). The measured results show that the filter chip is of high roll-off and stopband suppression. Most of the stopband suppression is better than 35 dB. Finally, error analysis was conducted, and FBAR parameters were modified after testing for future filter design work.

**Keywords:** radio frequency (RF) filter; mobile communication; film bulk acoustic resonator (FBAR); bulk wave filter (BAW); resonator model fitting



**Citation:** Yang, Q.; Xu, Y.; Wu, Y.; Wang, W.; Lai, Z. A 3.4–3.6 GHz High-Selectivity Filter Chip Based on Film Bulk Acoustic Resonator Technology. *Electronics* **2023**, *12*, 1056. <https://doi.org/10.3390/electronics12041056>

Academic Editor: Djuradj Budimir

Received: 13 January 2023

Revised: 15 February 2023

Accepted: 17 February 2023

Published: 20 February 2023



**Copyright:** © 2023 by the authors. Licensee MDPI, Basel, Switzerland. This article is an open access article distributed under the terms and conditions of the Creative Commons Attribution (CC BY) license (<https://creativecommons.org/licenses/by/4.0/>).

## 1. Introduction

In recent years, mobile communication technology has developed rapidly. For example, RF front-end devices [1], including filters, power amplifiers, low-noise amplifiers, RF switches, etc., have played an important role in the process of signal transmission. From the perspective of mobile communication network development, RF technology now faces many challenges, including “wider frequency range”, “more serious mutual interference”, “more flexible bandwidth configuration”, and a “more complex modulation mode”. To solve these problems, RF devices in the physical layer need to have the characteristics of multiband operation, good filtering performance, and flexible configuration. After years of network construction and development, many kinds of network systems co-exist, such as 2G, 3G, 4G, and 5G systems, and the spectrum fragmentation problem is increasingly serious.

As its name implies, an RF filter is used to sift signal. A filter with excellent performance can ensure that the whole communication system is not subject to interference by clutter. In [2,3], the authors proposed some novel resonator structures and fabricated two low-pass filters with excellent performance. Regrettably, these filters were not suitable for mobile phones due to their size limitation. At present, in the mobile filter market, communication frequencies below 2 GHz are mainly dominated by SAW filters [4]. However, as people enter the era of 5G and the communication frequency is extended to sub-6G, SAW filters are not competent for the demand of 5G communication due to their physical performance limitations. To solve this problem, BAW filters fabricated by FBAR and LC filters fabricated by low-temperature cofired ceramic (LTCC) or integrated passive device (IPD) processes have been developed [5,6]. There is also a kind of technology called laterally excited bulk wave resonator (XBAR) that can work at higher frequencies and with a wider bandwidth [7,8]. However, these related devices are not yet commercially available. Their scopes of application are shown in Figure 1.

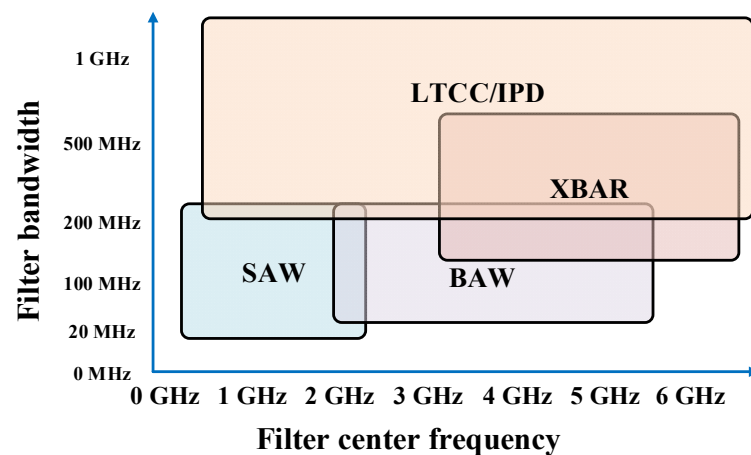


**Figure 1.** Mainstream technology and application frequencies of RF filters.

FBAR is a special microwave resonator with acoustic–electric conversion capability that is based on piezoelectric resonance theory and manufactured by microelectromechanical system (MEMS) film technology. The ideal airgap type of FBAR is a sandwich structure including an upper electrode, piezoelectric layer, lower electrode, and support layer. An airgap is etched between the silicon substrate surface and the lower electrode surface of the FBAR to form an air layer and an air reflection layer at the upper and lower interfaces of the FBAR resonator; therefore, a standing wave forms between the two air interfaces to limit the acoustic energy in the FBAR resonator. The equivalent electrical impedance expression of the FBAR resonator can be obtained from the joint solution of the classical acoustic eigen equation and Maxwell’s equations, called the Mason model.

At present, FBAR technology is widely used in the 4G and 4G+ bands, and there are still some problems when it comes to the application in the frequency range above the former. As the frequency of FBAR resonators increases, the effective area and the material thickness will decrease, resulting in the leakage of transverse acoustic energy, leading to the degradation of the resonator and filter performance. In terms of bandwidth, the frequency range between series and parallel resonators is limited by the dual resonant mode of acoustic resonators and the limited electromechanical coupling coefficient of piezoelectric materials, which leads to the problem that flexible bandwidth modulation cannot be easily achieved. The decrease in electrode layer thickness also leads to an increase in energy loss and a decrease in stopband suppression. Therefore, technological innovation is urgently necessary to facilitate the application of acoustic wave filters to 5G smart terminals.

In the last few years, there have been some studies on the extraction of piezoelectric material parameters [9–11] that have laid the groundwork for the calibration of the FBAR model and the design of filter circuits. In addition, there are some studies on SAW and BAW filters. In [12], a B1/B3 SAW quadruplexer was analyzed. In [13], a B3 FBAR duplex was analyzed and designed. However, most studies on such acoustic filters are limited to the traditional frequency band below 3 GHz. There is not much disclosed research on wideband acoustic filters in the n77, n78, and n79 bands. Meanwhile, most relevant papers are limited to the influence of material and element doping on the performance of a single resonator. Large manufacturers do not publish their data for reasons associated with patent protection. Thus, an example of complete filter chips is lacking.

In this paper, we designed a 3.4–3.6 GHz high-selectivity FBAR filter, which is exactly the working frequency of 4G LTE band 42. The iPhone 13 can now support communication in band 42. Furthermore, 3.4–3.6 GHz is the sub-band of n77 or n78. In China, this sub-band is used as a 5G communication frequency by China Unicom and China Telecom. In this paper, we screen and evaluate the performance of FBAR, design and analyze the filter schematic, the discuss the control method of transmission zeros (TZs), and present measurement results and data analysis of the filter chip.

## 2. Model Fitting of FBAR

In the design procedure of a transmission line filter and an LC filter, we will first carry out the schematic simulation in the ideal case, then draw the layout for EM simulation. The design process of the FBAR filter is roughly the same. However, we first need to obtain the theoretical model of a single FBAR in order to facilitate the following circuit topology design.

To this end, we use AlN with 9.6% scandium-doped concentration as the piezoelectric material. The doping of scandium element in AlN can improve the electromechanical coupling coefficient of the FBAR, which is more suitable to fabricate FBAR filters with a wider bandwidth. To acquire a suitable model for an FBAR at 3.5 GHz, we need to obtain the longitudinal acoustic velocities and densities of AlN and Mo using the method described in [11]. The physical structure and material of FBAR are shown in [14]; the modified Mason model used to fit an FBAR in [15] involves five layers, namely a seed layer (Seed), bottom electrode (BE), piezoelectric layer (PZ), top electrode (TE), and passive layer (PS). Table 1 shows these parameters of FBARs used to solve longitudinal acoustic velocities and densities of AlN and Mo. Finally, the calculation results are shown in Table 2.

**Table 1.** Parameters of the FBAR for model fitting.

	Seed (nm)	BE (nm)	PZ (nm)	TE (nm)	PS (nm)	$f_p^1$ (MHz)
Resonator 1	30.8	234.0	447.0	218.5	141.5	3217.2
Resonator 2	27.8	233.7	449.0	217.0	148.0	3231.6
Resonator 3	32.1	233.7	446.3	217.7	148.0	3220.0
Resonator 4	29.5	230.3	448.0	217.0	140.3	3223.8

<sup>1</sup> Parallel resonant frequency of FBAR.

**Table 2.** Modified longitudinal acoustic velocities and densities of AlN and Mo.

	Longitudinal Acoustic Velocity (m/s)		Density (kg/m <sup>3</sup> )	
	AlN	Mo	AlN	Mo
Original	10,886	5954	3270	9803
Modified	10,690.3	6240.7	3422.8	11,131.0

The performance prediction of the resonator and filter can be more accurate with an equivalent model that can accurately reflect the actual performance of the FBAR. The circuit design and circuit analysis can also be carried out on this basis.

## 3. Design and Analysis of the FBAR Filter

A Ladder type was chosen to realize the filter circuit. The working principle is that the low-frequency electrical signal is channeled to the ground by the minimum impedance point of the parallel FBAR resonator, thereby forming a transmission zero on the left side of the passband. The high-frequency electrical signal of the upper band is blocked by the maximum impedance of the series resonator. At the same time, a passband is generated by the resonance points falling within the passband. The passband of the filter can be adjusted by changing the thickness of each layer of the FBAR resonator. The Ladder type is beneficial to give full play to the advantage of sensitive frequency response characteristics of FBAR but also leads to a narrow bandwidth. Therefore, designers sometimes need to adopt appropriate methods to expand the bandwidth.

As shown in Figure 2, the circuit is composed of four series cells ( $S_{1,1}S_{1,2}$ ,  $S_{2,1}S_{2,2}$ ,  $S_{3,1}S_{3,2}$ , and  $S_{4,1}S_{4,2}$ ), five parallel cells ( $P_{1,1}P_{1,2}L_2$ ,  $P_2L_3$ ,  $P_3L_5$ ,  $P_4L_6$ , and  $P_{5,1}P_{5,2}L_7$ ), and three impedance-matching inductances ( $L_1$ ,  $L_4$ ,  $L_8$ ).  $S_{1,1}$  is the same as  $S_{1,2}$ .  $P_{1,1}$  is the same as  $P_{1,2}$ , etc. The red word "6K" in the figure means that the area of a single FBAR is 6000  $\mu\text{m}^2$ , and the remaining red words are the same. In addition, the thicknesses of each layer of the resonators are indicated in the figure. The thicknesses of Seed, BE, PZ, and PS are the same in all the FBARs.

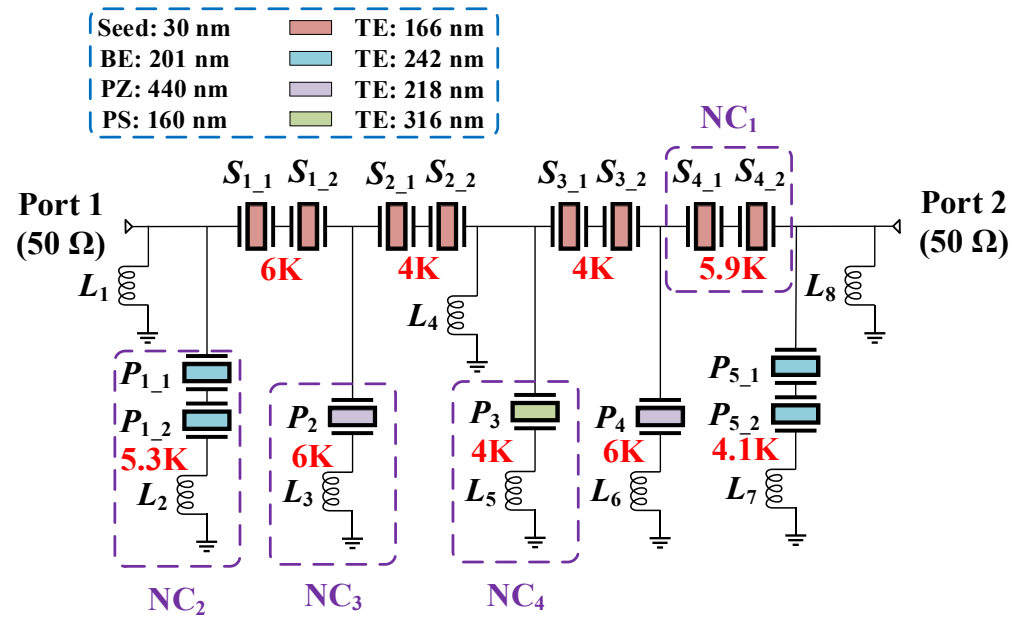


**Figure 2.** Topology of the FBAR filter ( $L_1 = 1.83$  nH,  $L_2 = 1$  nH,  $L_3 = 1$  nH,  $L_4 = 0.92$  nH,  $L_5 = 0.57$  nH,  $L_6 = 1$  nH,  $L_7 = 0.88$  nH,  $L_8 = 1.99$  nH).

To illustrate how the filter works, we can separate the whole circuit into 12 small network cells in series, which include three matching inductances, four series cells, and five parallel cells as mentioned above. Among them, network cell 1 (NC<sub>1</sub>) represents the network cell composed of  $S_{4,1}$  and  $S_{4,2}$ , and NC<sub>1</sub> can represent the performance of four series cells. NC<sub>2</sub>, NC<sub>3</sub>, and NC<sub>4</sub> are selected as representatives among the five parallel branches in consideration of the symmetry of the filter circuit.

To calculate the frequency response of the circuit, we first need to know the expression for the electrical properties of a single FBAR. In [14], the impedance expression of an FBAR under the equivalence of the Masson model is

$$Z_{\text{FBAR}} = \frac{1}{j\omega C_0 + (j(\omega C_0)^{-1} + N^2(-jZ_{\text{AIN}} \csc 2\theta + M))^{-1}}, \quad (1)$$

$$M = \frac{1}{(jZ_{\text{AIN}} \tan \theta + Z_t)^{-1} + (jZ_{\text{AIN}} \tan \theta + Z_b)^{-1}}, \quad (2)$$

$$N = \frac{2\theta}{k_t^2 \omega C_0 Z_{\text{AIN}}}. \quad (3)$$

where  $C_0$  is the static capacitance;  $Z_t$  and  $Z_b$  are the input impedances seen from the upper and lower surfaces of AlN, respectively;  $Z_{\text{AIN}}$  is the characteristic acoustic impedance of AlN;  $\theta$  is the phase shift of the longitudinal acoustic wave in AlN; and  $k_t$  is the electromechanical coupling coefficient of AlN.

After the impedance of a single FBAR is obtained, according to [16], the ABCD matrix of the four branches shown in Figure 3 can be written as

$$[A]_{\text{NC}_1} = \begin{bmatrix} 1 & Z_{S_{4,1}} + Z_{S_{4,2}} \\ 0 & 1 \end{bmatrix}, \quad (4)$$

$$[A]_{\text{NC}_2} = \begin{bmatrix} 1 & 0 \\ (Z_{P_{1,1}} + Z_{P_{1,2}} + j\omega L_2)^{-1} & 1 \end{bmatrix}, \quad (5)$$

$$[A]_{NC_3} = \begin{bmatrix} 1 & 0 \\ (Z_{P_2} + j\omega L_3)^{-1} & 1 \end{bmatrix}, \tag{6}$$

$$[A]_{NC_4} = \begin{bmatrix} 1 & 0 \\ (Z_{P_3} + j\omega L_5)^{-1} & 1 \end{bmatrix}. \tag{7}$$

where  $Z_{S_{4_1}} = Z_{S_{4_2}}$ , and  $Z_{P_{1_1}} = Z_{P_{1_2}}$ . The ABCD matrices of the remaining eight cascaded branches can be obtained by the same method. The ABCD matrix of the whole filter is the product of these 12 branches, which means

$$[A]_0 = \underbrace{[A]_{L_1} [A]_{NC_2} \cdots [A]_{L_8}}_{12 \text{ marixes}}. \tag{8}$$

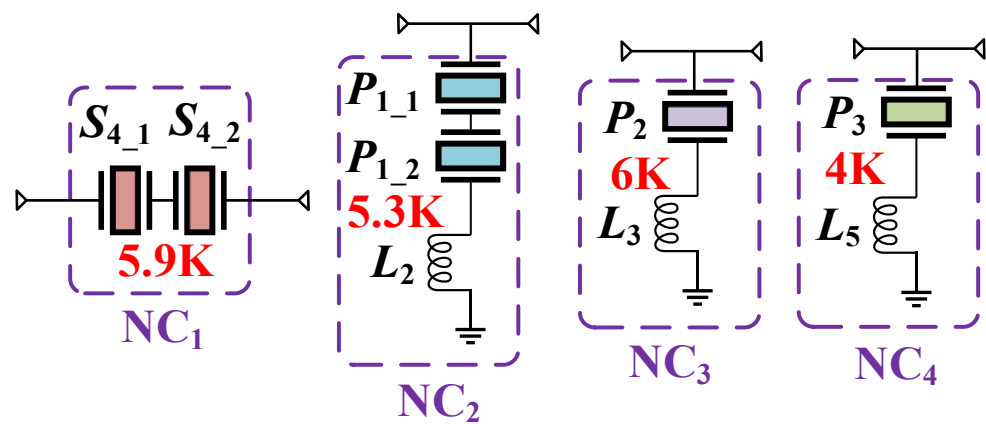


Figure 3. Cascaded branches NC<sub>1</sub>, NC<sub>2</sub>, NC<sub>3</sub>, and NC<sub>4</sub>.

After the ABCD matrix of the whole filter is calculated, according to [16], the conversion relationship between the S parameters and the ABCD matrix of the two-port reciprocal lossless network is

$$S_{11} = \frac{A + B/Z_0 - CZ_0 - D}{A + B/Z_0 + CZ_0 + D'} \tag{9}$$

$$S_{21} = \frac{2}{A + B/Z_0 + CZ_0 + D'} \tag{10}$$

$$S_{12} = \frac{2(AD - BC)}{A + B/Z_0 + CZ_0 + D'} \tag{11}$$

$$S_{22} = \frac{-A + B/Z_0 - CZ_0 + D}{A + B/Z_0 + CZ_0 + D}. \tag{12}$$

From this, we can obtain the S-parameter expressions of the whole filter. The frequency response of the filter is calculated by incorporating the parameters of each component into the expressions. The frequency responses of other branches are acquired in the same way, as shown in Figure 4.

To understand the characteristics of TZs, we first take NC<sub>1</sub> and NC<sub>3</sub> as representatives for analysis. Combining (4), (6), and (10), we can obtain

$$S_{21NC_1} = \frac{2Z_0}{2Z_0 + Z_{S_{4_1}} + Z_{S_{4_2}}} = \frac{Z_0}{Z_0 + Z_{S_{4_1}}}, \tag{13}$$

$$S_{21NC_3} = \frac{2(Z_{P_2} + j\omega L_3)}{Z_0 + 2(Z_{P_2} + j\omega L_3)}. \tag{14}$$

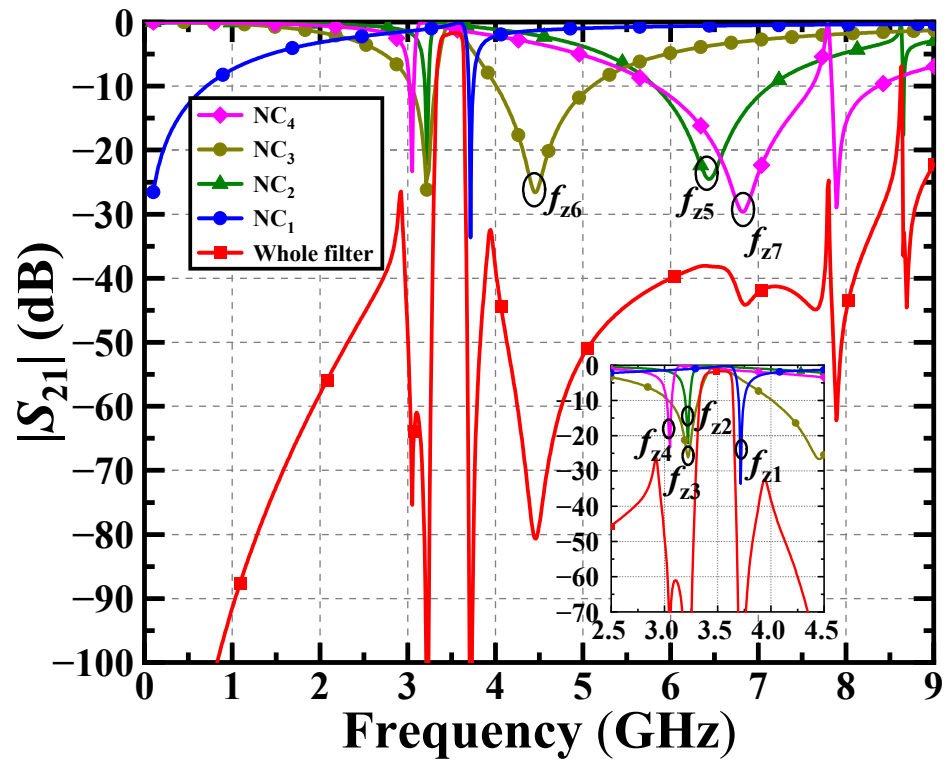


Figure 4. The frequency responses of the filter and branches.

Set  $S_{21NC_1} = 0$  and  $S_{21NC_3} = 0$ ; then

$$Z_{S_{4_1}} \rightarrow \infty, \tag{15}$$

$$Z_{P_2} + j\omega L_3 = 0 \Leftrightarrow j\omega L_3 = -Z_{P_2}. \tag{16}$$

Since the impedance expression (1) of FBAR involves many parameters, it is difficult to directly solve (15) and (16), but we can use the methodology of number-shape combination to understand the solutions visually. Functions  $g$  and  $y$  are introduced as

$$g = -\text{Im}(Z_{\text{FBAR}}), \tag{17}$$

$$y = \text{Im}(j\omega L) = \omega L. \tag{18}$$

The variation trend of  $g$  and  $y$  vs. frequency can be obtained as shown in Figure 5. As can be seen from the figure, there are two asymptotes (the asymptotes occur periodically as the frequency increases), where the impedance goes to infinity, and these frequencies represent the solutions for (15). In addition,  $g$  and  $y$  have at least two noteworthy intersections that represent the solutions for (16).

The TZs of the filter are highly consistent with the TZs of the branch cells when it comes to FBAR filters. The near-passband TZs are provided by acoustic resonance of FBARs.  $f_{z1}$  is provided by  $NC_1$  and other three-series cells.  $f_{z2}$  is provided by  $NC_2$  and its symmetric branch,  $P_{5_1}P_{5_2}L_7$ .  $f_{z4}$  is provided by  $NC_3$  and its symmetric branch,  $P_4L_6$ .  $f_{z4}$  is provided by  $NC_4$ . In addition, there are some TZs located at high frequencies due to the capacitive effect of FBARs, which resonate with series inductances, such as  $f_{z5}, f_{z6}, f_{z7}$ , etc. These TZs ensure suppression at high frequencies.

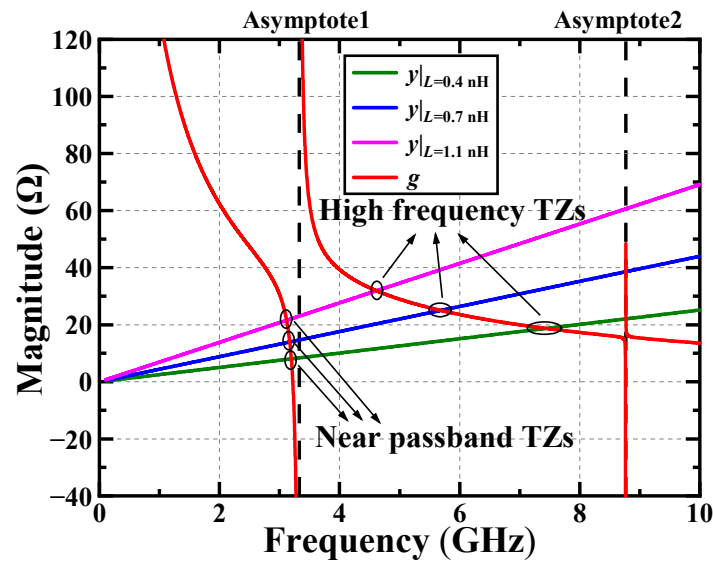


Figure 5. The variation trend of  $g$  and  $y$  vs. frequency.

#### 4. EM Simulation and Measured Results

Layout modeling and electromagnetic simulation are carried out after the theoretical analysis is completed. The EM simulation is supported by HFSS simulation software. The 3D EM model and the laminate layers of the filter are shown in Figures 6 and 7, respectively. The filter consists of two parts: the FBAR die and the laminate fabricated by coreless technology. These two parts are merged by flip chip (FC) technology. Silicon via (TSV) and bump are the connecting holes in this case. As for the laminate, the multilayer metal and via used for coil inductance is copper and other filling dielectrics are Fr-4. Figure 7 shows the structural details of the laminate. The laminate has five metal layers, which are named Top, M2, M3, M4, and Bottom. The adjacent layers are connected by via holes. Each of the four images contains two metal layers and the via hole. The bottom layer has three metal plates, which serve as the input port, output port, and ground. The size of the chip is  $1.1 \times 0.9 \times 0.5 \text{ mm}^3$ .

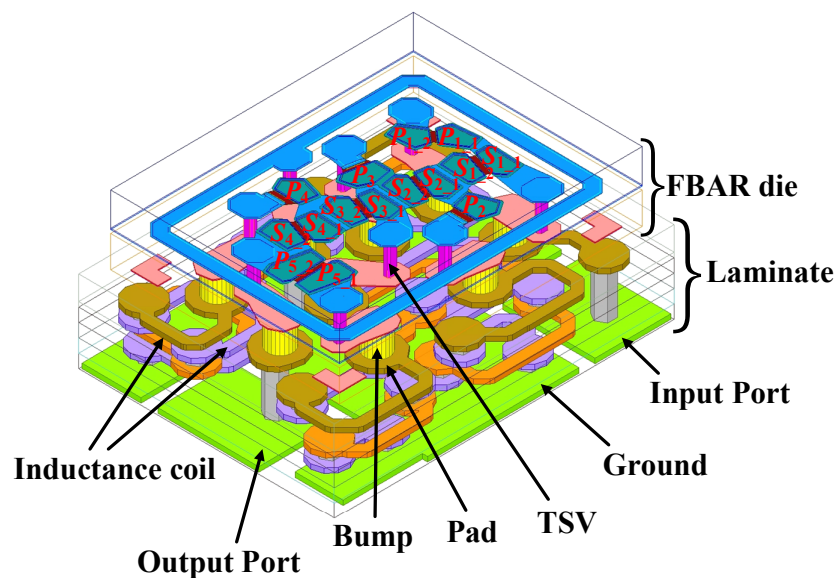


Figure 6. The 3D model of the filter chip ( $1.1 \times 0.9 \times 0.5 \text{ mm}^3$ ).

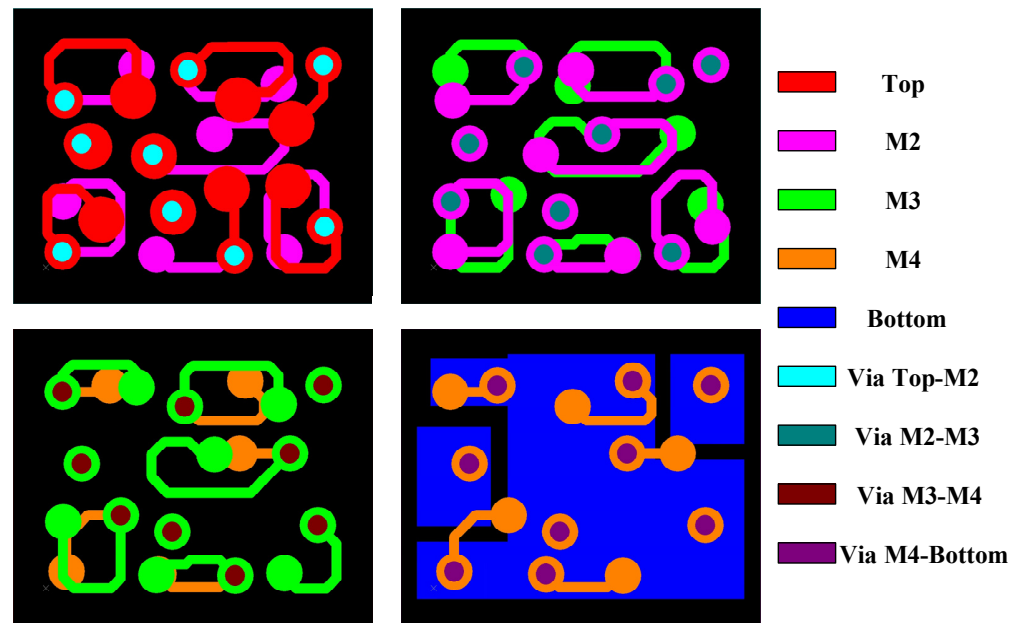


Figure 7. Laminate layers of the filter chip.

The chip is installed on the evaluation board (EVB) for testing, as shown in Figure 8a. Figure 8b shows the test environment. The upper and lower parts of the evaluation board are identical, which can be used to install two chips. This time, we use the upper part. Figure 9 shows the simulated results and measured results of the filter chip. The measured results exhibit a certain deterioration compared with the simulated results. The best measured insertion loss is 2.5 dB at 3.56 GHz. The insertion loss is 3.58 dB at 3.4 GHz and 3.21 dB at 3.6 GHz. The measured return loss is better than 12 dB in the passband. In addition, several representative mobile communication bands above 2 GHz located in the stopband are marked in Figure 9 for visual comparison, including B40, 2.4G Wi-Fi, B41, N41, N79, and 5G Wi-Fi.

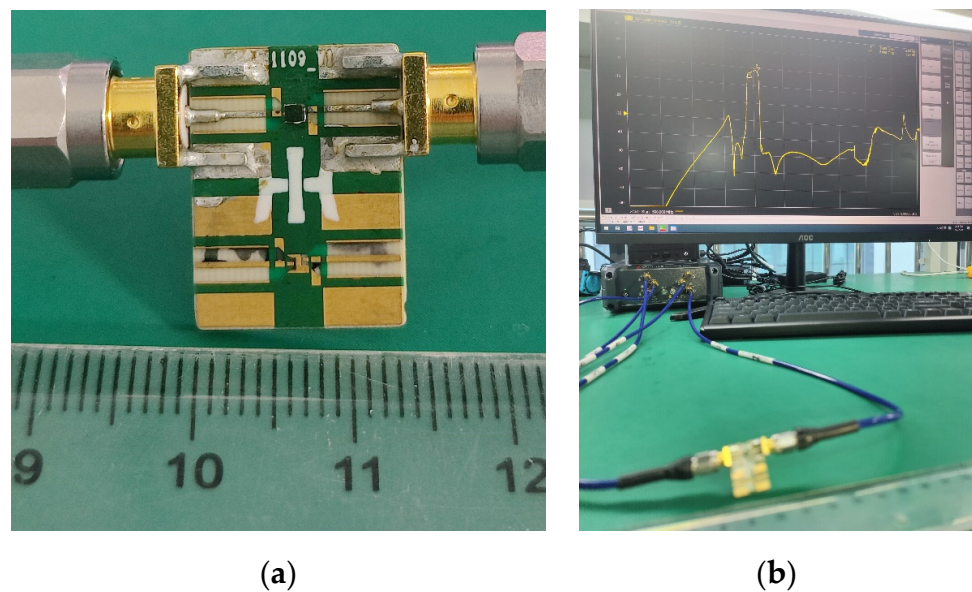


Figure 8. The fabricated filter chip and test environment. (a) Filter chip on EVB. (b) Test environment.

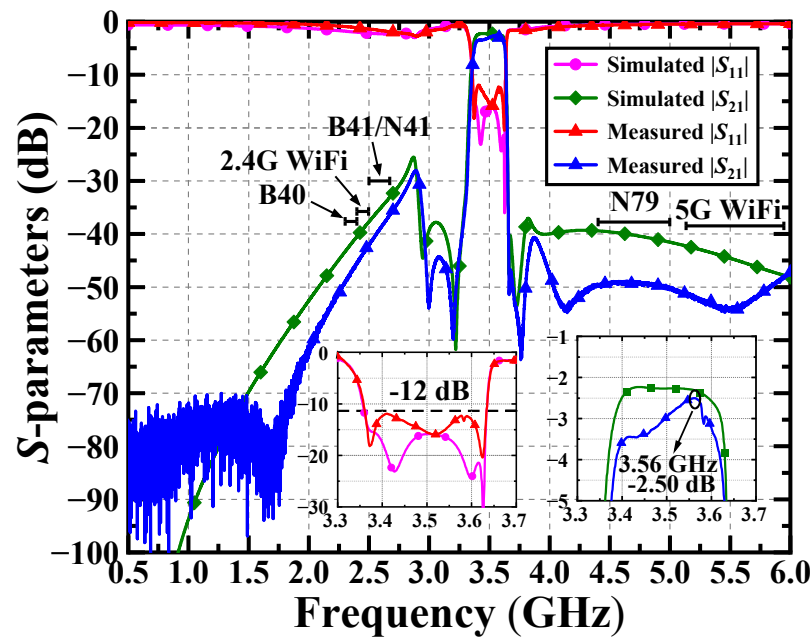


Figure 9. Simulated and measured results of the filter chip.

In order to analyze the error of simulated and measured results, we need to select several individual resonators to test.  $S_{1-1}$  and  $S_{2-1}$  were tested and compared with the simulated results, as shown in Table 3. Obviously, the  $kt_{eff}$  values of the measured resonators are larger; the magnitude of the error for  $S_{1-1}$  is 0.008, and that for  $S_{2-1}$  is 0.0029. As for the other resonators, there will also be errors, which will deteriorate the passband matching. At the same time, the quality factor ( $Q$ ) of the resonators decreased, and the reductions in  $Q_s$  and  $Q_p$  of the two resonators vary from 200 to 700, leading to the deterioration of passband insertion loss (IL). In addition,  $f_s$  and  $f_p$  of the resonators are slightly biased, leading to the deterioration of the passband matching. After this, we carried out scandium-doped concentration analysis of piezoelectric material AlN. The test results show that the actual scandium-doped concentration is 6% rather than 9.6%, which is also one of the reasons that causes errors. Thus, process accuracy improvement requires more efforts.

Table 3. Comparison of simulated and measured performance of a single FBAR.

	$kt_{eff}^1$	$f_s^2$ (GHz)	$f_p^3$ (GHz)	$Q_s^4$	$Q_p^5$
Measured $S_{1-1}$	0.0845	3.547	3.672	278	960
Simulated $S_{1-1}$	0.0765	3.598	3.717	784	1385
Measured $S_{2-1}$	0.0794	3.578	3.701	425	733
Simulated $S_{2-1}$	0.0765	3.598	3.717	665	1407

<sup>1</sup> Equivalent electromechanical coupling coefficient of FBAR. <sup>2</sup> Series resonant frequency of FBAR. <sup>3</sup> Parallel resonant frequency of FBAR. <sup>4</sup> Series quality factor of FBAR. <sup>5</sup> Parallel quality factor of FBAR.

This is the first scandium-doped AlN design working above 3 GHz proposed by our company, and the FBAR model and simulated accuracy still need to be improved. According to analysis,  $kt_{AlN}$  was adjusted from 7.61% to 7.38%. Some other parameters of the model were also adjusted. The modified parameters can better fit the measured results and lay a foundation for the next design work.

Table 4 shows the comparative performance of several acoustic filters in recent years.

**Table 4.** Several acoustic filters and their performance.

Ref.	Type	$f_c^1$ (GHz)	IL <sup>2</sup> (dB)	BW <sup>3</sup> (MHz)	FOM <sup>4</sup>	Stopband Suppression <sup>5</sup> (dB)	Size
[17]	FBAR	3.71	3.04	120	30.92	37	$1.25 \times 0.9 \text{ mm}^2 / 0.015 \times 0.011 \lambda_0^2$
[18]	FBAR	2.6	1.7	120	21.67	35	$1.1 \times 0.9 \text{ mm}^2 / 0.0095 \times 0.0078 \lambda_0^2$
[19]	FBAR	2.45	2.5	150	16.33	25	$1.1 \times 0.9 \text{ mm}^2 / 0.0089 \times 0.0074 \lambda_0^2$
[20]	XBAR	3.55	1.4	120	29.58	30	$1 \times 1 \text{ mm}^2 / 0.012 \times 0.012 \lambda_0^2$
[21]	SAW	3.44	1.3	200	17.2	30	
[22]	SAW	3.74	3.03	500	7.48	20	
This work	FBAR	3.52	3.1	200	17.6	35	$1.1 \times 0.9 \text{ mm}^2 / 0.013 \times 0.011 \lambda_0^2$

<sup>1</sup> Center frequency. <sup>2</sup> Average insertion loss in passband. <sup>3</sup> Passband bandwidth. <sup>4</sup> Figure of Merit. <sup>5</sup> average level of stopband suppression.

## 5. Conclusions

In this paper, an FBAR filter for the frequency range of 3.4–3.6 GHz was designed, analyzed, and fabricated. The design procedure was explained, including FBAR performance fitting, filter schematic analysis, and the generation principle of TZs. A visual mathematical model was presented so that transmission zeros are easier to understand. Finally, an FBAR filter chip was fabricated and tested for verification. The measured results show that the filter chip has high roll-off, high-frequency selectivity, and good stopband suppression. There are some differences between the measured results and the simulated results but within the expected range. The analysis work can almost explain the error. Furthermore, the resonator model parameters were modified to prepare for the next design work.

**Author Contributions:** Conceptualization, Q.Y. and Z.L.; methodology, Q.Y., Y.X. and Z.L.; software, Q.Y. and Z.L.; validation, Q.Y. and Y.X.; formal analysis, Q.Y. and Y.X.; investigation, Q.Y. and Y.X.; resources, Q.Y., Y.W., W.W. and Z.L.; data curation, Q.Y. and Y.X.; writing—original draft preparation, Q.Y. and Y.X.; writing—review and editing, Q.Y., Y.X., Y.W., W.W. and Z.L.; visualization, Y.X.; supervision, Z.L.; project administration, Z.L.; funding acquisition, Y.W. and W.W. All authors have read and agreed to the published version of the manuscript.

**Funding:** This work was supported by the National Natural Science Foundations of China (Nos. U20A20203 and U21A20510) and the Fundamental Research Funds for the Central Universities (2021XD-A07-2).

**Data Availability Statement:** The data presented in this study are available within the article.

**Acknowledgments:** In this section, we acknowledge Haopeng Wu, Xiaojie Tian, and Xun Cai for technical support during the experiments. We also acknowledge Lei Huang for providing editing and writing assistance.

**Conflicts of Interest:** The authors declare no conflict of interest.

## References

- Li, Z.; Cheng, G.; Wang, Z. A 0.1–1 GHz low power RF receiver front-end with noise cancellation technique for WSN applications. *AEU—Int. J. Electron. Commun.* **2018**, *83*, 288–294. [\[CrossRef\]](#)
- Roshani, S.; Dehghani, K.; Roshani, S. A Lowpass Filter Design Using Curved and Fountain Shaped Resonators. *Frequenz* **2019**, *73*, 267–272. [\[CrossRef\]](#)
- Hookari, M.; Roshani, S.; Roshani, S. Design of a low pass filter using rhombus-shaped resonators with an analytical LC equivalent circuit. *Turk. J. Electr. Eng. Comput. Sci.* **2020**, *28*, 865–874. [\[CrossRef\]](#)
- Psychogiou, D.; Gómez-García, R.; Peroulis, D. Single and Multiband Acoustic-Wave-Lumped-Element-Resonator (AWLR) Bandpass Filters with Reconfigurable Transfer Function. *IEEE Trans. Microw. Theory Tech.* **2016**, *64*, 4394–4404. [\[CrossRef\]](#)
- Hao, L.; Wu, Y.; Wang, W.; Yang, Y. Design of On-Chip Dual-Band Bandpass Filter Using Lumped Elements in LTCC Technology. *IEEE Trans. Circuits Syst. II Express Briefs* **2022**, *69*, 959–963. [\[CrossRef\]](#)
- Xu, Y.; Wu, Y.; Wu, H.; Yang, Y.; Wang, W. Wideband High Selectivity Filter Chips with Adjustable Bandwidth Based on IPD Technology. *IEEE Trans. Circuits Syst. II Express Briefs* **2022**, *69*, 4273–4277. [\[CrossRef\]](#)
- Yandrapalli, S.; Plessky, V.; Koskela, J.; Yantchev, V.; Turner, P.; Villanueva, L.G. Analysis of XBAR resonance and higher order spurious modes. In Proceedings of the IEEE International Ultrasonics Symposium, Glasgow, UK, 6–9 October 2019.

8. Plessky, V.; Yandrapalli, S.; Turner, P.J.; Villanueva, L.G.; Koskela, J.; Faizan, M.; De Pastina, A.; Garcia, B.; Costa, J.; Hammond, R.B. Laterally excited bulk wave resonators (XBARS) based on thin Lithium Niobate platelet for 5GHz and 13 GHz filters. In Proceedings of the IEEE MTT-S International Microwave Symposium, Boston, MA, USA, 2–7 June 2019.
9. Lee, S.; Lee, V.; Sis, A.; Mortazawi, A. A simple nonlinear mBVD model parameter extraction method for intrinsically switchable ferroelectric FBARs. In Proceedings of the European Microwave Integrated Circuit Conference, Nuremberg, Germany, 6–8 October 2013.
10. Yokoyama, T.; Iwazaki, Y.; Onda, Y.; Nishihara, T.; Ueda, M. Highly piezoelectric co-doped AlN thin films for wideband FBAR applications. *IEEE Trans. Ultrason. Ferroelectr. Freq. Control* **2015**, *62*, 1007–1015. [[CrossRef](#)] [[PubMed](#)]
11. Wu, H.; Cai, X.; Wu, Y.; Lai, Z.; Yang, Q.; Wang, W. An investigation on extraction of material parameters in longitudinal mode of FBAR. *IEEE Trans. Circuits Syst. II Express Briefs* **2020**, *67*, 1024–1028. [[CrossRef](#)]
12. Ruby, R.; Gilbert, S.; Lee, S.K.; Nilchi, J.; Kim, S.W. Novel Temperature-Compensated, Silicon SAW Design for Filter Integration. *IEEE Microw. Wirel. Compon. Lett.* **2021**, *31*, 674–677. [[CrossRef](#)]
13. Wu, Y.; Wu, H.; Wang, W.; Yang, Y.; Lai, Z.; Yang, Q. A Compact Low-Loss High-Selectivity Excellent-Isolation FBAR Duplexer Integrated Chip for LTE Band-3 Industrial Applications. *IEEE Trans. Circuits Syst. II Express Briefs* **2022**, *69*, 4563–4567. [[CrossRef](#)]
14. Wu, H.; Wu, Y.; Lai, Z.; Wang, W.; Yang, Q. A Hybrid Film-Bulk-Acoustic-Resonator/Coupled-Line/Transmission-Line High Selectivity Wideband Bandpass FBAR Filter. *IEEE Trans. Microw. Theory Tech.* **2020**, *68*, 3389–3396. [[CrossRef](#)]
15. Jamneala, T.; Bradley, P.; Koelle, U.B.; Chien, A. Modified Mason model for bulk acoustic wave resonators. *IEEE Trans. Ultrason. Ferroelectr. Freq. Control* **2008**, *55*, 2025–2029. [[CrossRef](#)] [[PubMed](#)]
16. Pozar, D.M. *Microwave Engineering*, 2nd ed.; Wiley: New York, NY, USA, 1997.
17. Shealy, J.B.; Vetry, R.; Gibb, S.R.; Hodge, M.D.; Patel, P.; McLain, M.A.; Feldman, A.Y.; Boomgarden, M.D.; Lewis, M.P.; Hosse, B.; et al. Low loss, 3.7 GHz wideband BAW filters, using high power single crystal AlN-on-SiC resonators. In Proceedings of the IEEE MTT-S International Microwave Symposium, Honolulu, HI, USA, 4–9 June 2017.
18. Gu, J.; Wu, Y.; Lai, Z.; Wu, H.; Wang, W.; Yang, Y. An N41-Band Bandpass BAW Filter Chip for Mobile Communications Based on FBARs. In Proceedings of the 2020 IEEE Asia-Pacific Microwave Conference, Hong Kong, China, 8–11 December 2020.
19. Bogner, A.; Bauder, R.; Timme, H.J.; Forster, T.; Reccius, C.; Weigel, R.; Hagelauer, A. Enhanced Piezoelectric AL1–XSCXN RF-MEMS Resonators for Sub-6 GHz RF-Filter Applications: Design, Fabrication and Characterization. In Proceedings of the 2020 IEEE 33rd International Conference on Micro Electro Mechanical Systems, Vancouver, BC, Canada, 18–22 January 2020.
20. Shen, Y.; Zhang, R.; Vetry, R.; Shealy, J. 40.6 Watt, High Power 3.55 GHz Single Crystal XBAW RF Filters for 5G Infrastructure Applications. In Proceedings of the IEEE International Ultrasonics Symposium, Las Vegas, NV, USA, 7–11 September 2020.
21. Kimura, T.; Omura, M.; Kishimoto, Y.; Hashimoto, K. Comparative Study of Acoustic Wave Devices Using Thin Piezoelectric Plates in the 3–5-GHz Range. *IEEE Trans. Microw. Theory Tech.* **2019**, *67*, 915–921. [[CrossRef](#)]
22. Su, R.; Fu, S.; Shen, J.; Lu, Z.; Xu, H.; Wang, R.; Song, C.; Zeng, F.; Wang, W.; Pan, F. Wideband Surface Acoustic Wave Filter at 3.7 GHz with Spurious Mode Mitigation. *IEEE Trans. Microw. Theory Tech.* **2022**, *71*, 480–487. [[CrossRef](#)]

**Disclaimer/Publisher’s Note:** The statements, opinions and data contained in all publications are solely those of the individual author(s) and contributor(s) and not of MDPI and/or the editor(s). MDPI and/or the editor(s) disclaim responsibility for any injury to people or property resulting from any ideas, methods, instructions or products referred to in the content.